Modeling river bed morphology, roughness, and surface sedimentology using high resolution terrestrial laser scanning

J. Brasington,[1,2] D. Vericat,[3] and I. Rychkov[2]

[1]   Recent advances in technology have revolutionized the acquisition of topographic data, offering new perspectives on the structure and morphology of the Earth's surface. These developments have had a profound impact on the practice of river science, creating a step change in the dimensionality, resolution, and precision of fluvial terrain models. The emergence of "hyperscale" survey methods, including structure from motion photogrammetry and terrestrial laser scanning (TLS), now presents the opportunity to acquire 3-D point cloud data that capture grain-scale detail over reach-scale extents. Translating these data into geomorphologically relevant products is, however, not straightforward. Unlike traditional survey methods, TLS acquires observations rapidly and automatically, but unselectively. This results in considerable "noise" associated with backscatter from vegetation and other artifacts. Moreover, the large data volumes are difficult to visualize; require very high capacity storage; and are not incorporated readily into GIS and simulation models. In this paper we analyze the geomorphological integrity of multiscale terrain models rendered from a TLS survey of the braided River Feshie, Scotland. These raster terrain models are generated using a new, computationally efficient geospatial toolkit: the topographic point cloud analysis toolkit (ToPCAT). This performs an intelligent decimation of point cloud data into a set of 2.5-D terrain models that retain information on the high-frequency subgrid topography, as the moments of the locally detrended elevation distribution. The results quantify the degree of terrain generalization inherent in conventional fluvial DEMs and illustrate how subgrid topographic statistics can be used to map the spatial pattern of particle size, grain roughness, and sedimentary facies at the reach scale.

Citation: Brasington, J., D. Vericat, and I. Rychkov (2012), Modeling river bed morphology, roughness, and surface sedimentology using high resolution terrestrial laser scanning, *Water Resour. Res.*, *48*, W11519, doi:10.1029/2012WR012223.

1.   Introduction

[2] Accurate digital models of river channel topography are fundamental tools in river science. They provide the morphological boundary conditions for numerical hydrodynamic simulations and baselines to quantify erosion and sedimentation and estimate sediment transport rates [*Ashmore and Church*, 1998; *Bates et al.*, 2003; *Brasington et al.*, 2003]. Quality topographic data are also key to the assessment of physical habitat [*Richards et al.*, 2002; *Wheaton et al.*, 2010a] and through multitemporal surveys can provide insights into fluvial morphodynamics; improving our understanding of climate, land use, and extreme events as drivers of channel change [e.g., *Eaton and Lapointe*, 2001; *Williams et al.*, 2011].

[3] The production of fluvial topographic data has, over the last two decades, been revolutionized through advances in survey platforms and instrumentation, alongside innovations in computational algorithms, software, and hardware. These developments have facilitated the acquisition of dense, distributed topographic data through rapid ground surveys with GPS and robotic tacheometry but perhaps more fundamentally through the growing range of earth observation technologies such as softcopy photogrammetry, structure from motion, airborne LiDAR, interferometric radar and multibeam echo sounding [*Gao*, 2009; *Marcus and Fonstad*, 2010]. This progress has enabled a profound shift in the dimensionality of terrain data and the progressive replacement of cross-sectional representations of channels and floodplains by digital elevation models or DEMs. These spatially continuous data structures are ideally suited to higher-dimensional hydraulic modeling [*Horritt and Bates*, 2002; *McMillan and Brasington*, 2007] and are directly compatible with geospatial software to facilitate spatially distributed geomorphic change detection [*Brasington et al.*, 2000; *Lane*, 2005; *Wheaton et al.*, 2010b].

[4] The fierce pace of technological growth has continued to widen the scope and quality of topographic surveys; stretching the extent of data acquisition and the density of

---

[1]Queen Mary, University of London, London, UK.
[2]University of Canterbury, Christchurch, New Zealand.
[3]University of Lleida, Lleida, Spain.

Corresponding author: J. Brasington, Queen Mary, University of London, London E1 4NS, UK. (j.brasington@qmul.ac.uk)

observations, alongside continual improvements in horizontal and vertical precision and accuracy. Consequently, a variety of methods now exist to collect data with sufficient coverage and resolution to quantify the full spectrum of fluvial morphologies, from grain-to-network scale, as shown schematically in Figure 1.

[5] While individual technologies can be targeted to particular applications precisely, Figure 1 reveals the difficulty of acquiring data that transcend this scale continuum and help reveal how the particle-scale building blocks of the fluvial system are aggregated and organized to create macromorphologies. For example, airborne LiDAR is an ideal tool to map the three-dimensional structure of bar forms and their reach-scale distribution, but with a typical observation density of ~ 1 point m^{-2} and a vertical precision in the decimeter range is generally unsuitable to characterize particle or bed form morphologies (10^{-2}–10^{0} m) and detect subtle bed changes. By contrast, a detailed ground survey using a total station offers an useful alternative at such fine scales (e.g., to capture ripple/dune morphology or particle cluster spacing), however the intensive labor involved limits the practical extent of surveys much beyond the bar scale (10^{1}–10^{2} m).

[6] An important consequence of this "scale gap" is the entrenchment of the methodological separation of "large-scale" topography and "small-scale" roughness implicit in conventional approaches to hydraulic and morphodynamic modeling. This separation of scales has hindered the development of physically based models of fluid-boundary interaction that conjoin the topographic controls on flow resistance, blocking, and steering [*Lane*, 2005]. The difficulty of quantifying topography continuously has instead encouraged the parameterization of fine-scale grain and form resistance through quasi-analytical functions (e.g., roughness

lengths or coefficients) or visual assessment [*Barnes*, 1967; *Hicks and Mason*, 1991], while flow blocking and steering are resolved only at coarser scales, explicitly through a scale-dependent topographic boundary condition.

[7] Methods that use multiscale topographic data to represent both these effects on flow resistance, notably porosity-based treatments of the solid boundary, have begun to emerge as novel parameterization strategies for numerical hydrodynamic models [e.g., *Lane et al.*, 2004; *Yu and Lane*, 2006; *McMillan and Brasington*, 2007; *Casas et al.*, 2010]. Such approaches offer an elegant means of reconciling the mismatching scales of computationally affordable model discretizations and finer topographic controls, however, their application remains severely limited by the availability of appropriate topographic data.

[8] Continuing technical developments are now poised to meet this challenge with the advent of ruggedized, terrestrial laser scanners. Employing similar physical principles to those used in airborne LiDAR, these ground-based instruments can acquire unprecedented volumes of survey-grade observations, generating very dense point cloud data sets with subcentimeter point spacing and precision. Terrestrial laser scanning (hereafter TLS) for the first time offers the opportunity to construct landscape-scale (10^{2}–10^{4} m) DEMs seamlessly at the resolution of the fundamental particle scale (10^{-3}–10^{-1} m) building blocks (Figure 2).

[9] Applications of TLS in the earth and environmental sciences are beginning to gather momentum, with applications across a wide range disciplines from volcanology [e.g., *James et al.*, 2009] and slope stability [e.g., *Dunning et al.*, 2010; *Aryal et al.*, 2012] to vegetation dynamics [e.g., *Danson et al.*, 2007]. The use of TLS in river science is similarly expanding rapidly, but to date has been limited typically to small-scale, very high resolution geometrical
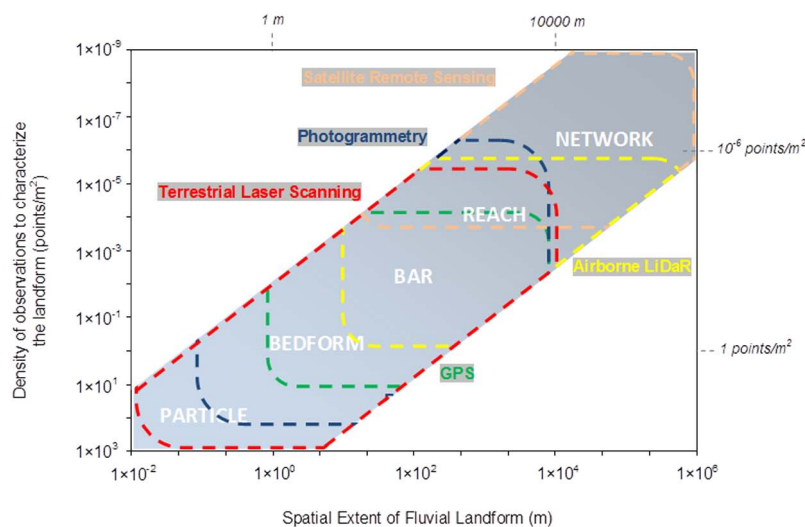

Figure 1. The overlapping capabilities of geospatial technologies used to characterize fluvial systems. The necessary survey density refers the minimum number of observations required to characterize each landscape scale. For example, the geometry of a river reach is typically described by the long profile and can therefore is often measured from a set of thalweg elevations acquired at intervals of many tens of meters (10^{-6} pts m^{-2}), but extending over a large areas (10^{3}–10^{4} m). Terrestrial laser scanning can be used to derive information relevant to parameterize the fluvial system from grain-to-reach within one single data set.
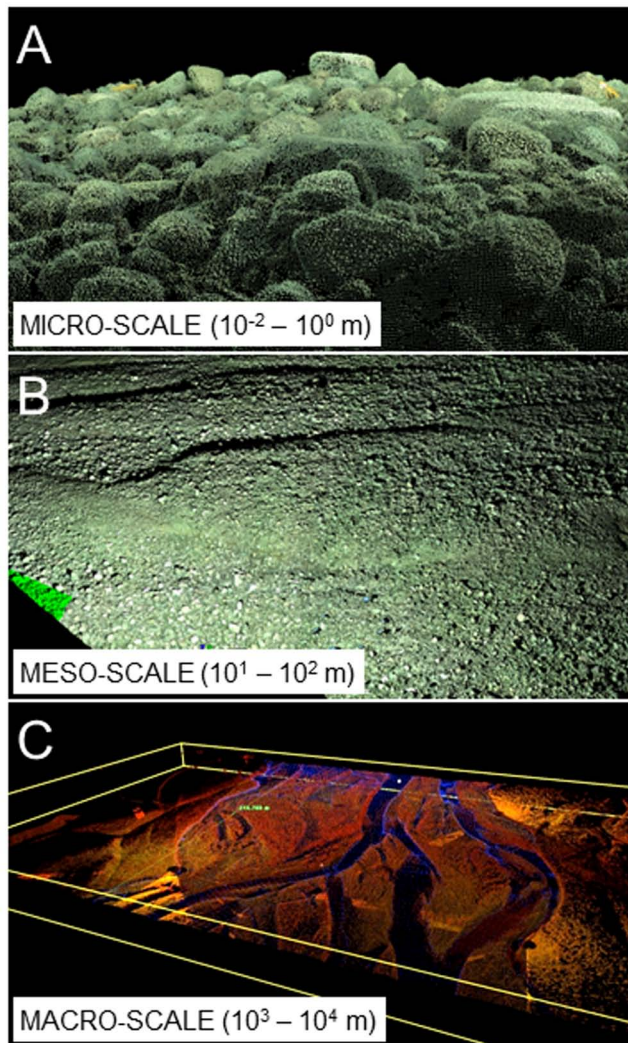
Figure 2. Seamless topographic modeling of the fluvial system derived by terrestrial laser scanning. Three views of the same point cloud revealing multiscale perspectives afforded through TLS survey.

modeling. For example, recent applications have included the measurement of the explicit grain-scale packing and sorting characteristics of gravel beds [*Hodge et al.*, 2009a, 2009b; *Wang et al.*, 2011; *Wang and Huang*, 2012]; the kinematics of individual bars [*Milan et al.*, 2007]; and the development of new parameterizations of vegetative flow resistance based on high resolution scans of floodplain plants and trees [*Antonarakis et al.*, 2009, 2010]. This restricted use in part reflects difficulties involved in the field capture of data, which until recently has involved the integration of slow, individual scans requiring many hours of ground occupation to acquire wide-area coverage. However, continuing enhancements in scanner speed and more significantly the emergence of kinematic scanning systems that integrate TLS with inertial or optical navigation solutions and enable the deployment of TLS from mobile platforms, are set to dramatically enhance the spatial extent of data coverage [e.g., *Barber et al.*, 2008; *Alho et al.*, 2009; *Brasington*, 2010; *Williams et al.*, 2011].

[10] However, in addition to the logistical difficulties of field data collection, the adoption of TLS is hindered more significantly by a range of generic data management problems that arise from the sheer scale of the data sets generated. Large area scans [e.g., >3 km^2 see, for example, *Williams et al.*, 2011] may incorporate as many as 10^7–10^9 individual *xyz* observations; volumes well beyond the processing capacity of standard desktop GIS, CAD, and visualization software. In addition, there are further key concerns over the assessment of data quality; the management of image "noise" resulting from instrument artifacts and unselective spatial sampling; the derivation of relevant data products; and their optimal assimilation within a simulation modeling or change detection framework.

[11] Here we seek to address some of these issues by presenting a geospatial toolkit, ToPCAT (topographic point cloud analysis toolkit) designed specifically to analyze very large TLS data sets and generate terrain data sets suitable for hydraulic modeling and change detection. The approach involves an intelligent decimation of the raw scan data into reduced-resolution gridded elevation models that retain high-frequency topographic information from the point cloud as the moments of the locally detrended elevation distribution. Further details of the computational methods used to implement this scheme are presented by *Rychkov et al.* [2012].

[12] In this paper we apply ToPCAT to a large (approximately 1000 × 300 m) TLS data set acquired on the braided River Feshie, Scotland in 2007 and undertake a detailed geomorphic analysis of the derived terrain products. This involves: (1) an examination of DEM quality based on the topographic complexity of terrain models derived over a range of grid resolutions (0.1–10 m); (2) a comparison of TLS-derived DEMs with a conventional lower resolution GPS-based data set; and (3) the assessment of an automated particle size and facies model based on the locally detrended standard deviation of elevation. While the techniques presented here are examined specifically within the context of TLS data, the same methods could be applied equally to other emerging dense survey methods, such as multibeam echo sounding or structure from motion photogrammetry [*Westoby et al.*, 2012].

2. Terrestrial Laser Scanning

[13] Terrestrial laser scanners (Figure 3a) are active laser imaging systems that combine high frequency laser range observations with precision angular sampling to generate spatially dense point cloud data [*Lichti et al.*, 2008; *Petrie and Toth*, 2008]. Designed originally for applications in civil and structural engineering, portable, full-dome (360° × 270° field of view) TLS have since been enthusiastically adopted within a range of fields, including architecture, transport, heritage, archaeology, mining, and forensic science [*Vosselmann and Mass*, 2010]. Applications across the geosciences are now beginning to emerge rapidly as instrumentation costs fall and awareness of the capability of TLS grows (see *Buckley et al.* [2008] and *Heritage and Large* [2009] for recent reviews).

[14] While prototype TLS were first developed in the 1990s, fast, ruggedized instrumentation suitable for field-based geophysical survey has only become available in the
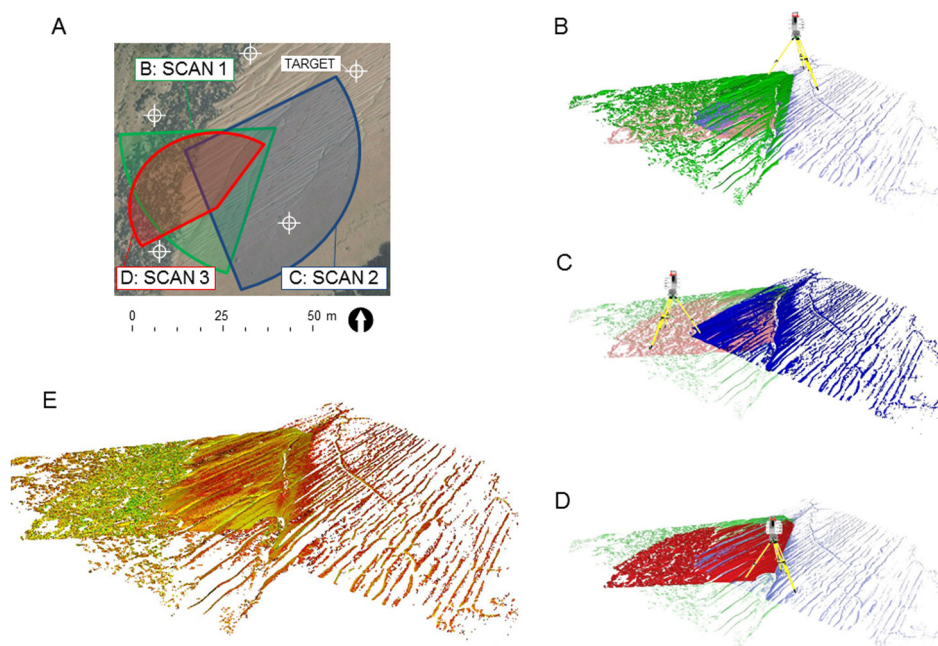
Figure 3. Registering TLS data from multiple setups. (a) A typical study site; exposed estuarine mudflats scanned from (b–d) three positions at low tide to capture the morphology of complex mud bed forms visible trending NE-SW. The highlighted point clouds in Figures 3b–3d are registered using a network of intravisible targets (Figure 3a) to integrate the survey into a single data set which captures the (e) complex bed form geometry not visible from a single setup. The final product (Figure 3e) is rendered using the intensity of the backscatter return.

last 3–4 years. In these systems, 3-D measurements are facilitated by a sensor head comprising rotating mirrors, servo-motors and accurate radial encoders that enable fine angular measurement (μrad–mrad) and dense spatial sampling across a wide field of view. For example, a typical 100 μrad sampling interval at a range of 100 m equates to 10 mm point spacing and a density of 10,000 pts m^{-2}.

[15] Distance measurement is based on reflections from natural objects without the need for retroreflectors and uses either time-of-flight or continuous-wave (phase-difference) ranging [*Wehr and Lohr*, 1999]. Time-of-flight scanners operate typically over longer distances (10–4000 m) but at significantly reduced measurement frequencies (2–50 kHz). By contrast, continuous-wave devices acquire data at very fast rates and therefore at high densities, but generally only over short ranges (typically <40–180 m). Until recently most scanners returned single range estimates along a given bearing, based on the last significant reflector (or last pulse). The next generation of scanners now coming to market, however, offer the capacity to discretize the returned waveform into multiple reflections providing information on the opacity of the scene. For both approaches, range errors are strongly linked to divergence of the laser beam and (without secondary compensation) verticality of the sensor head, so that point accuracy deteriorates with distance [*Lichti and Jamtsho*, 2006]. In effect, a trade-off between data quality (spatial density and point accuracy) and range emerges that must be tailored to the particular application and field logistics.

[16] Currently available instruments operate over ranges of tens of meters to >4 km and at measurement frequencies

of between 1 and 1000 kHz (1000–1,000,000 pts s^{-1}). Most scanners also record the intensity of the reflected laser beam, which although strongly influenced by distance, incidence angle, and surface moisture, may also provide information on surface mineralogy and roughness [*Lichti*, 2005; *Franceschi et al.*, 2009, *Nield and Wiggs*, 2011]. Additionally, some instruments incorporate high-resolution digital cameras, enabling the true-color pixel values to be remapped directly onto each survey observation to produce photo-realistic 3-D renderings. Further technical details on the principles of TLS are available elsewhere [e.g., *Wehr and Lohr*, 1999; *Lichti et al.*, 2002].

[17] Terrestrial laser scanners are generally deployed on a tripod and held stationary for the duration of measurements at a fixed position. Most scanners have rotating sensor heads and scanning mirrors that create a 360° horizontal field of view along with wide, even overhead, vertical sampling. Despite this large sampling window, data acquisition remains limited by line-of-sight, so that surveys of complex objects typically require multiple setups to ensure adequate overlap and coverage (Figure 3). The observables from each position are a set of measurements of range, horizontal and vertical angles, and intensity. These are converted directly to local Cartesian coordinates (x, y, z) where the origin and orientation are defined relative to an internal scanner coordinate system (scanner space).

[18] Two important steps are thus required for the production of data deliverables; registration and georeferencing. Registration refers to the merging of multiple scans into a common unified, but relative coordinate system, whereas georeferencing involves the transformation of

scans to an established local, national, or global coordinate system (object space). These two processes are often referred to synonymously, but represent important distinct processes which incorporate different sets of errors.

[19] Registration of multiple scans can be achieved using either or a combination of two approaches: (1) a rigid body similarity (conformal) transformation from scanner-space to object-space based on common, observed control points identified by reflective targets [e.g., *Horn*, 1987] or (2) cloud-to-cloud registration which involves identifying tie points between overlapping point clouds on the basis of local matching geometry. This latter approach utilizes the large redundancy that exists in dense scan data and a variety of methods have been developed to solve this complex problem (e.g., the iterative closest point algorithm of *Besl and McKay* [1992] [see also *Lichti and Skaloud*, 2010]). In practice these two approaches are often best used in combination, whereby a 3-D similarity transformation based on known targets is used to provide the initial orientation of the point clouds, then cloud-to-cloud registration employed to maximize the fit. Registration is also best undertaken as a global transformation problem, where multiple overlapping scans are orientated simultaneously and global least-squares metrics used to ensure the isotropy of the solution.

[20] While registration of scan data to a common, relative coordinate system may be sufficient to generate products suitable for characterizing a particular object, it is often desirable to tie these data to a recognized frame of reference. This step facilitates the integration of additional data, such as airborne LiDAR or ground observations positioned by GPS and importantly also enables the comparison of data sets over time. Georeferencing is usually undertaken during post-processing as part of registration, where control points measured on national or global mapping system are used to define the principal similarity transformation. Direct (forward) georeferencing during data collection is also possible when the location and orientation of the sensor head are prescribed a priori and the scan observables (range and angles) are transformed directly. This approach is likely to become more popular as new instruments directly incorporate GPS and inertial measurement units, so enabling the collection of real-world coordinates in real time. Finally, it is important to recognize that georeferencing inevitably introduces uncertainties associated with the accuracy of the positional data used to define transformations and that care should be taken to work within a consistent 3-D Cartesian framework to avoid incorporating distortion associated with map projections.

3. Digital Elevation and Subgrid Modeling

[21] TLS data have largely been modeled by generating 3-D watertight models by meshing directly the raw scan data [e.g., *Antonarakis et al.*, 2009] or by fitting known geometric primitives to point clouds. While this can deliver rich, complex geometrical models, meshing very large point clouds is computationally demanding, requires substantial manual editing, and is therefore, appropriate only for small-scale applications or simple geometries. The resulting 3-D data structures are, moreover, not easily assimilated into existing 2-D hydrodynamic models nor readily compatible with GIS software with their rich variety of tools for visualization and terrain analysis.

[22] Simplification of the 3-D point data (x,y,z) to a 2.5-D terrain model function $z = f(x,y)$, either as rasters or triangular irregular networks (TINs) therefore remains a practical alternative for the processing and subsequent redistribution, analysis, and assimilation of landscape-scale data sets. The extraction of 2.5-D DEMs from unselectively sampled scan data is not straightforward however and requires segmentation of the point cloud to distinguish "ground" and "off-terrain" points [*Heritage and Hetherington*, 2007]. Although this distinction is comparatively unambiguous for the smooth surfaces of the built environment [e.g., *Priestnall et al.*, 2000; *McMillan and Brasington*, 2007], rough natural surfaces such as a gravelly river bed exhibit significant topographic variability across a range of scales; from individual particles to small sedimentary structures, up to aggregate bar forms. Recently, *Brodu and Lague* [2012] have demonstrated how higher-order analysis of the 3-D structure of point cloud data may offer a means to classify scan data into complex categories such as gravel surfaces, boulders, and vegetation. However, while their approach holds significant potential, a simple means to decimate even classified point clouds are nonetheless required to aid the assimilation of dense spatial data within numerical models and GIS.

[23] Here we present a new geospatial algorithm designed for processing very large TLS data sets, the topographic point cloud analysis toolkit, or ToPCAT. This is used to extract multiresolution terrain products and a set of complementary statistical surfaces which retain information on the locally detrended subgrid topography. This approach enables significant data simplification without wholesale loss of information and is capable of processing multibillion observation point clouds on a standard desktop computer, running a 64-bit operating system.

[24] The workflow used to process a 3-D point cloud is presented graphically in Figure 4. Formally, we take the point cloud to be an unstructured set S of n points in $\Re 3$, sampled from a 2.5-D elevation function, $z(x,y)$. Methods to reconstruct this function by interpolation are well established, however the computational complexity of these methods (e.g., inverse-distance weighting, spline fitting, Kriging) limits their application to comparatively small data problems $(n < 10^6)$. An alternative strategy is to decompose the plane containing the points into a set of nonoverlapping segments, each containing a smaller number of points and then to interpolate each segment independently. Stage 1 of the processing methodology (Figure 4) therefore uses a 2-D "bucket sort" algorithm [*Weiss*, 2007] which segments S into regularly sampled square domains (gridcells) of extent $\Delta X \Delta Y$ and computes the set of points in each gridcell and its neighbors. This sorting algorithm is linear in time and was implemented in C++ using 64-bit optimization and memory caching to support very large data sets.

[25] The points in each gridcell are then themselves sorted and instead of direct local interpolation, the moments of the elevation distribution are sampled and the precise coordinates of the minimum and maximum elevation points identified (stage 2). A variety of terrain functions can then be interpolated from this reduced resolution data set, taking either statistical measures of z, e.g., $\min(z)$, $\mathrm{mean}(z)$, $\max(z)$, σ_z assumed to lie at the cell centroid, or using
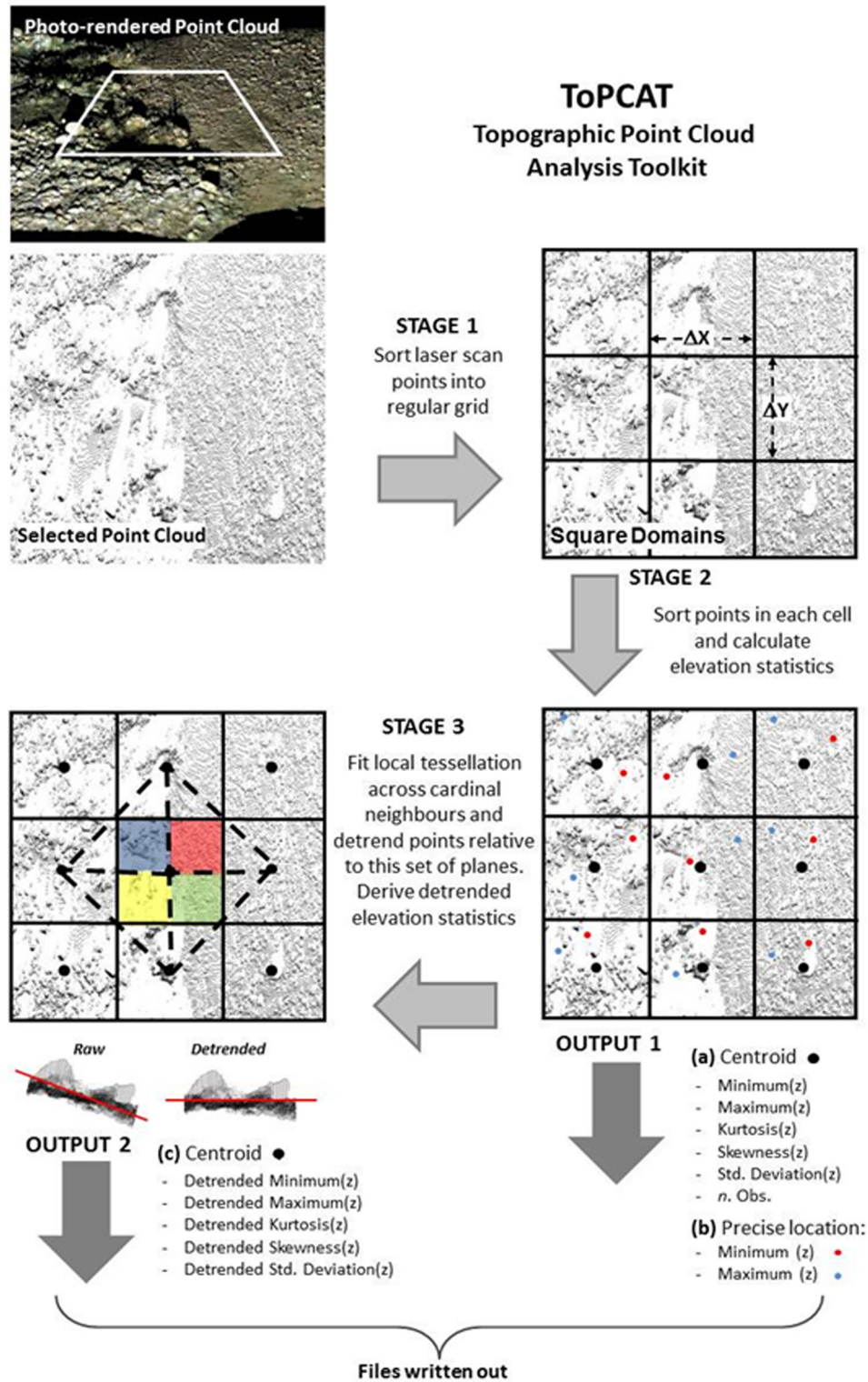
Figure 4. The ToPCAT workflow: A geostatistical toolbox to filter 3-D point cloud data.

min(z) or max(z) based on their precise (subgrid) locations (output 1).

[26] A simple, neighborhood triangular tessellation is then used to reconstruct the surface locally, fitting four planes to elevation measures at the centroids of the principal and adjacent cardinal cells (stage 3). While more complex interpolators could be used, this approach has two advantages. First, user selection of a particular z attribute for the tessellation, such as the minimum elevation allows a deliberate bias to help reduce the effects of unwanted reflections

from vegetation or surface objects. Second, the tessellation is a hydrologically continuous surface rather than a set of disjointed, locally fitted planes. In the final step of the workflow, the tessellation is used to detrend all points within the central gridcell and a new set of statistical moments and sampled elevations (min, max, and mean) are extracted (stage 4 and output 2). This second set of attributes therefore reflects variability found within each gridcell after removal of spatial trends, such as bank edges and avalanche slopes which are larger than the grid resolution.

[27] This spatial sorting process provides a simple but intelligent decimation of the point cloud and can be implemented at any resolution that balances sample frequency, topographic complexity, and user goals. Multiple DEM products can then be derived at each scale, for example, using the minimum or maximum local elevations to represent extreme topographies, or surfaces representing the distribution of the subgrid elevation statistics. The C++ source code, libraries, and binaries are available for free download under a GNU general public license agreement at http://code.google.com/p/point-cloud-tools. The code is called by a Python script and expects an input file as *x,y,z* flat text and can be used in batch mode to automatically generate gridded products across a range of resolutions. The outputs are flat text files directly compatible with ArcGIS.

4. Case Study Data Collection: The Braided River Feshie

[28] The study area is a 1 km long braided reach of the River Feshie that drains an 80 km^2 watershed within the Cairngorm Mountains, Scotland (Figure 5). The channel bed comprises schistose, cobble-sized material (D_{50} varies between 50 and 110 mm). The braidplain is largely inundated in moderate floods (mean annual flood = 70 m^3 s^{-1}), however, during low flows between 85% and 90% of the channel bed is subaerially exposed and discharge confined in two to three shallow anabranches (mean depth 0.4 m). This is significant, as the eye-safe (class 1–3R) lasers used in most TLS are not water penetrating. Thus, while ideally suited for data collection in braided rivers, TLS in common with many other remote sensed survey methods (e.g., airborne LiDAR) may have more limited use in widely inundated fluvial systems. While not discussed here, the development of continuous channel bed models even for braided rivers requires infilling of this submerged topography, either with ground-based or remotely sensed bathymetry [see, e.g., *Brasington et al.*, 2003; *Westaway et al.*, 2003; *Williams et al.*, 2011].

[29] Data acquisition was completed during low flow conditions ($Q = 1.4$ m^3 s^{-1}) in July 2007. Two independent topographic surveys were obtained, first with multistation TLS and second with real time kinematic GPS to provide a conventional, benchmark topographic data set.

4.1. TLS Survey

[30] Scans were undertaken with a Leica ScanStation: a pulsed 532 nm laser scanner, with a 360° × 270° field of view, a maximum range of 300 m (at 90% reflectivity) and an operating frequency of 2–4 kHz. The scanner was mounted on a heavy-duty tripod at approximately 2 m height
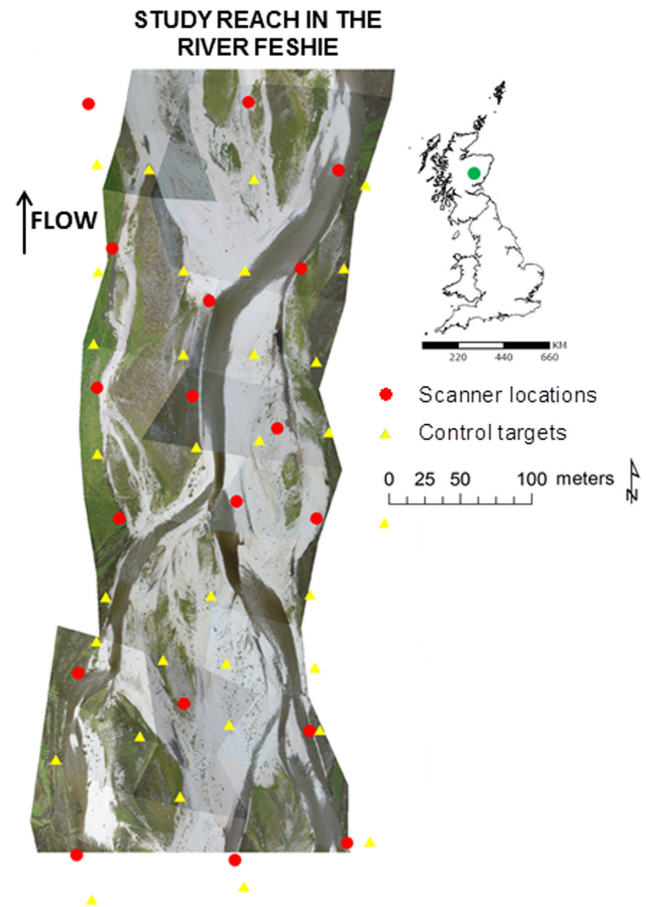

Figure 5. Survey network revealing scan stations and control target locations used to acquire TLS data of the study reach, the River Feshie, Scotland, in 2007.

and controlled from a laptop PC in the field running the Leica Geosystem TLS control and modeling software *Cyclone*. This allows data to be visualized live during acquisition and has controls to specifically target regions, acquire registration targets, and modify the scan resolution. Both laptop and scanner were powered using a smoothed output EU10i Honda generator.

[31] The theoretical accuracy of the scan data varies with distance due to the propagation of angular errors and laser beam divergence. Manufacturer specifications suggest a 3-D point precision of 6 mm (1 σ) at 50 m. Contiguous coverage of the study reach required 18 survey stations, spaced at between 80 and 100 m (Figure 5b). At each location, a full 360° scan was obtained with the resolution set to a point spacing of 15 mm at a range of 30 m. The actual point spacing is higher closer to the scanner and decays linearly with distance. Line of sight losses (due to vegetation and shadowing by the dissected topography) required careful positioning of each survey station to maximize data returns.

[32] The scans were registered and georeferenced using a global 3-D similarity transformation estimated using least-squares adjustment in *Cyclone*. The transformation was calculated using a network of 43 independent tripod-mounted, retroreflective survey targets, each tied to local planar approximation of the UK OSGB36 coordinate system by GPS. A minimum of four targets were visible from

each scan location and 200 coincident links used to define the global transformation, while a subset of 46 links were used to provide an independent assessment of the transformation. The mean absolute transformation errors were found to be: 7 mm in xy ($\sigma = 6$ mm) and 7 mm in z ($\sigma = 7$ mm) for control links, rising to only 9 and 7 mm ($\sigma = 9$ and 9 mm), respectively, when evaluated against the independent check data. The resulting point cloud comprised 326 million observations with a mean density of over 1765 pts m^{-2} and a mean point spacing of 13 mm. The point density is however highly variable, with a maximum of 390,822 pts m^{-2} recorded in areas close to the scanner, while 2.2% of the study reach had between 1 and 4 observations at a 1 m sampling resolution and 2.3% recorded no observations at all, although these were small discrete locations of shadow.

[33] Prior to further processing, the point cloud was cleaned manually within the visualization environment of Cyclone, and large trees and the targets were clipped from the scan and the area of interest restricted to a 700 m central reach. These steps reduced the resulting point cloud to 178 million points. No attempt was made to remove the sporadic cover of low-level vegetation, largely grasses and heather (*Calluna vulgaris* and *Erica cinerea*), with the intention of using the minimum elevation attribute to help create "bare-earth" surfaces. In addition to off-terrain observations caused by surface features, a variety of other scan artifacts are evident in the data set, including observations in midair, due to dust and insects and multipath reflections close to the waters' edge. Obvious examples of such artifacts were also removed by visual inspection, although some observations were inevitably overlooked due to the complexities of rendering the complete scene. A visualization of the point cloud is shown in Figure 6, where the points are colored with RGB values obtained from an integrated camera.

4.2. GPS Survey

[34] The study reach was also surveyed using real time kinematic (RTK) GPS to provide a reference, comparison data set against which to benchmark the TLS models. Following *Brasington et al.* [2000], observations were acquired in rapid stop-and-go mode using Leica 1200 series GPS, with a 3-D error tolerance set at 40 mm. The total survey (requiring 14 man days) comprised 34,266 observations with an internally estimated mean 3-D point quality of 17 mm and observation density of 0.17 pts m^{-2} ($\sigma = 0.14$ m). These data were transformed on to the same coordinate system as the TLS survey. The observations were interpolated using Delaunay triangulation and then resampled on to a 1 m resolution DEM, following protocols established by prior surveys on the Feshie and documented at length elsewhere [see *Brasington et al.*, 2000, 2003; *Wheaton et al.*, 2010a]. A 1 m resolution has been adopted for similar GPS surveys of the study site and reflects a compromise between the density of support observations and the apparent local topographic complexity. The DEM quality was assessed using a bootstrap test, randomly separating 5% of the survey observations as check data and performing a grid-to-point comparison. This found a standard deviation of absolute errors ($|Z_{GPS} - Z_{DEM}|$) of 0.1 m, a mean (signed) error of <0.01 m, and revealed no visually identifiable systematic errors or blunders.
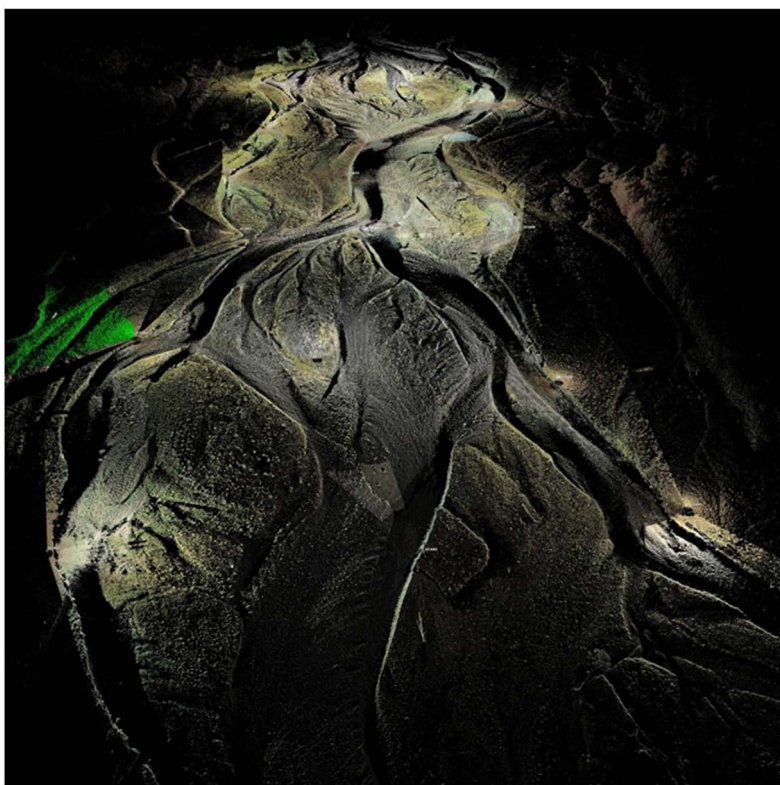

Figure 6. Photo-rendered point cloud of the study reach, comprising 178 million observations.

5. DEM Quality Assessment

[35] The clipped TLS point cloud was processed using ToPCAT (Figure 4) and grids of the raw and locally detrended elevation statistics were extracted at 0.1, 0.25, 0.5, 0.75, 1, 2, 5, and 10 m resolutions. Small shadows (typically <1–2 m^2) caused by line of sight losses, most evident in the highest resolution grids, were interpolated by Delaunay triangulation and then resampled to the same raster resolution. In the first instance, the minimum elevation was used to derive the terrain surface, under the assumption that this value relates to laser returns that have penetrated the sparse vegetation cover. Following extraction, each DEM was adjusted to remove the average valley slope (1.1%). This emphasizes the drainage structure of the DEM, but this differs from the local, neighborhood detrending undertaken by ToPCAT. Descriptive statistics for the detrended DEMs, along with the 1 m resolution model derived from the GPS survey are presented in Table 1.

[36] Two approaches were used to investigate DEM quality: (1) an evaluation of topographic complexity as grid resolution was degraded progressively from 0.1 to 10 m and (2) a comparison of a coarse resolution TLS-based DEM (1 m) with a comparable surface derived from the significantly less dense GPS point cloud (based on four orders of magnitude less support data).

5.1. Scale-Dependent Topographic Complexity

[37] Prior to the advent of TLS, fluvial topographic DEMs have rarely exceeded meter resolution for areas larger than small, individual bars. The extreme density of observations provided by TLS now provides an opportunity to examine the additional information and complexity recorded as DEM resolution is increased, ultimately toward the scale of individual particles (0.1–0.25 m). Here the topographic complexity was assessed using three different geospatial metrics: (a) the surface rugosity; (b) the frequency distribution of local slope angles; and (c) the reach-averaged topographic relief.

5.1.1. Rugosity

[38] Rugosity is a 3-D measure of the topographic roughness or complexity defined as

$$f_r = \frac{A_s}{A_p}, \tag{1}$$

where f_r is the rugosity (dim.), A_s is the 3-D surface area, and A_p is the planimetric or 2-D area (both m^2). This parameter is particularly sensitive to local variability in surface slope and aspect and the presence of topographic singularities (peaks and pits). Rugosity was estimated by fitting an 8-plane tessellation across a moving 3×3 cell neighborhood and truncating this to cover only the central cell [see *Jenness*, 2004]. The area of the set of planes was then summed to predict A_s and equation (1) calculated taking A_p as the grid resolution. The local statistics were then aggregated to give a regional average and spatial standard deviation. The relationships between the average and standard deviation of rugosity with DEM resolution are plotted in Figure 7. As expected, the shallow fluvial topography results in low rugosity values (<1.1) for all DEMs compared with, for example, crenulated, mountain landscapes [see *Grohmann et al.*, 2010]. However, a clear scaling pattern is evident, with rugosity falling rapidly from 1.045 at 0.1 m resolution to 1.009 m at 0.75 m, followed by a break in slope and more gradual loss of rugosity to 1.001 between 1 and 10 m resolutions.

5.1.2. Local Slope

[39] Fluvial topography is marked by sharp breaks of slope, cut banks, chutes, and avalanche faces, all of which are difficult to capture accurately and preserve as DEM resolution is degraded. In order to examine the potential loss of discontinuities, important for topographic steering of the flow and form resistance, the frequency distribution of slope angles was calculated for each DEM using the maximum local slope angle or D8 algorithm [see *Brasington and Richards*, 1998]. The resulting cumulative frequency distributions along with the median and quartile values are shown together in Figure 8. As expected, this shows the progressive loss of the distribution tail of high slopes and the translation of the entire distribution to lower values as the resolution is degraded. In common with the rugosity, the loss of terrain information is most evident between 0.1 and 0.75 m, over which the upper quartile slope angle falls from 9.9° to 5.1° and the median from 5.2° to 2.8°. The lower quartile also declines with grid size at a comparable rate, roughly proportional to the $\sqrt[3]{}$ of the grid size, suggesting a wholesale, progressive, flattening of the topography.

5.1.3. Surface Relief

[40] A measure of characteristic surface relief was computed by calculating the mean absolute deviation between each gridcell and the plane describing the fitted average valley slope. Note that as the TLS data do not include the wetted channel topography, the result is biased toward only the exposed topographic surfaces. The relationship between average relief and grid size is shown in Figure 9. Again, this function exhibits a rapid loss of information and a strong break of slope, here at 2 m resolution. Between 0.1 and 2 m relief falls rapidly from 0.51 to 0.31 m but much more slowly from 0.31 to 0.29 m between the 2 and 10 m resolutions.

5.1.4. Analysis of Results

[41] All geospatial metrics reveal a significant loss of topographic complexity as DEM resolution is degraded, with each indicator highlighting the rapidity of information loss between the 0.1 and 1 m grid sizes. This range accounted for 80% of the total lost rugosity, a rapid systematic translation in the distribution of slope angles in which the upper quartile slope falls from 9.9° at 0.1 m to 4.3° at 1.0 m resolutions, while over 20 cm of lost relief (>40% of the total) was recorded between the 0.1 and 2 m grids.

Table 1. Descriptive Statistics of the Detrended Digital Elevation Models at Different Grid Sizes

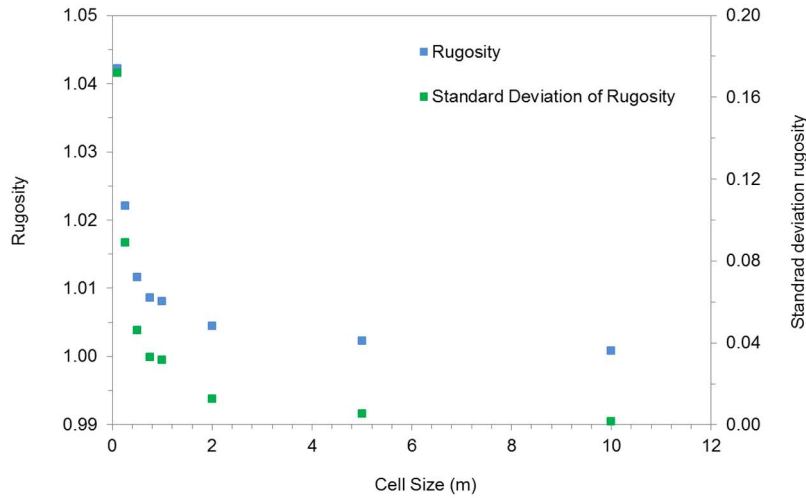| Grid Size (m) | Detrended Elevations | | | |
	Lowest (m)	Highest (m)	Height (m)	n Obs.
0.1	−3.75	2.05	5.80	8,228,144
0.25	−3.63	2.04	5.67	1,316,731
0.5	−3.63	1.67	5.30	329,187
0.75	−3.62	1.52	5.14	146,305
1	−3.69	1.57	5.26	82,298
2	−2.46	1.38	3.84	20,583
5	−2.74	1.24	3.98	3,304
10	−1.95	1.08	3.03	821

Figure 7. Relationship between rugosity, the standard deviation of rugosity, and TLS-derived DEM resolution.

[42] These effects can be explained by analyzing the spatial distribution of elevation differences between the DEMs as shown in Figure 10. Here the 0.5, 1.0, and 2.0 m models have been resampled to 0.1 m and the differences between these surfaces and the highest resolution model evaluated by grid-by-grid subtraction (i.e., $0.1-X$, where X is resolution of the coarser grid). The resulting difference maps reveal the subgrid scale topography lost as the output model is generalized. The most significant changes are evident around steep breaks of slope associated with bar-top chute channels and bank edges. This pattern is not simply an artifact of sampling frequency, but reflects the systematic choice of the minimum local elevation to build the DEM, chosen deliberately to help remove surface (vegetation) objects. As the grid size increases, the search area for this lowest value extends and the elevation value returned for the cell centroid becomes potentially more and more distant (horizontally) from the actual minimum. Ultimately this results in a progressive loss of relief, widening of channelized topography, and negatively biasing the elevation. This pattern is well illustrated by the extracted cross sections shown in Figure 10 which in turn explains the reduction in overall model relief identified in Figure 9.

[43] This loss of complexity has important consequences for both hydraulic modeling and change detection by DEM differencing. In the former case, the loss of fine-scale topography effectively reduces the surface volume of the topographic boundary. This is likely to enhance flow dispersion due to the lack of explicit topographic steering and blocking of the flow. In turn, this will to lead to overestimates of inundation area for a given discharge, but also a loss of extreme simulated depths and shear stresses with attendant implications for predictions of bed mobility. This chain of consequences is similar to that obtained directly
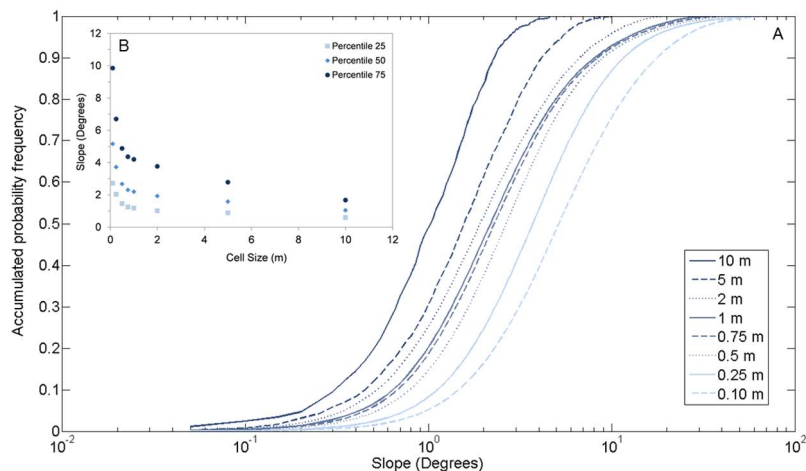

Figure 8. Cumulative frequency distributions of slope angles for grid resolutions between 0.1 and 10 m. The inset B summaries the relationship showing the median and quartiles of the slope distribution changing with DEM resolution.
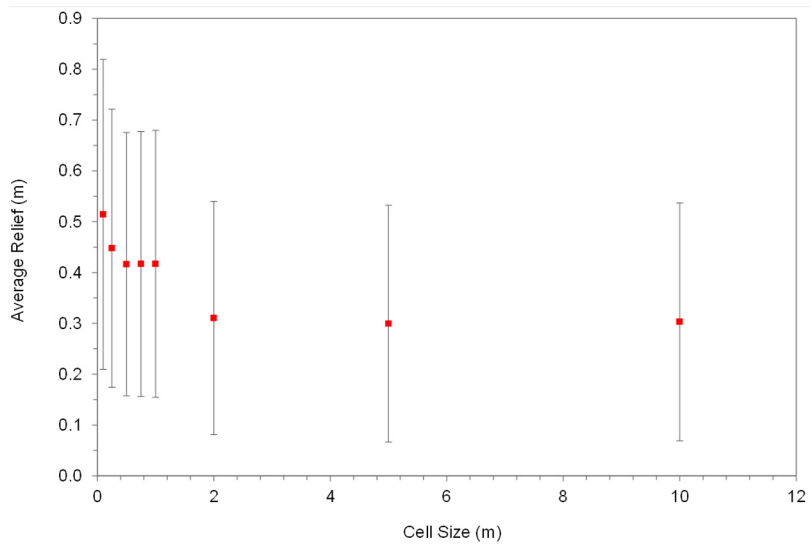
Figure 9.   Relationship between average relief and DEM grid size (variability shown by 1 s error bars).
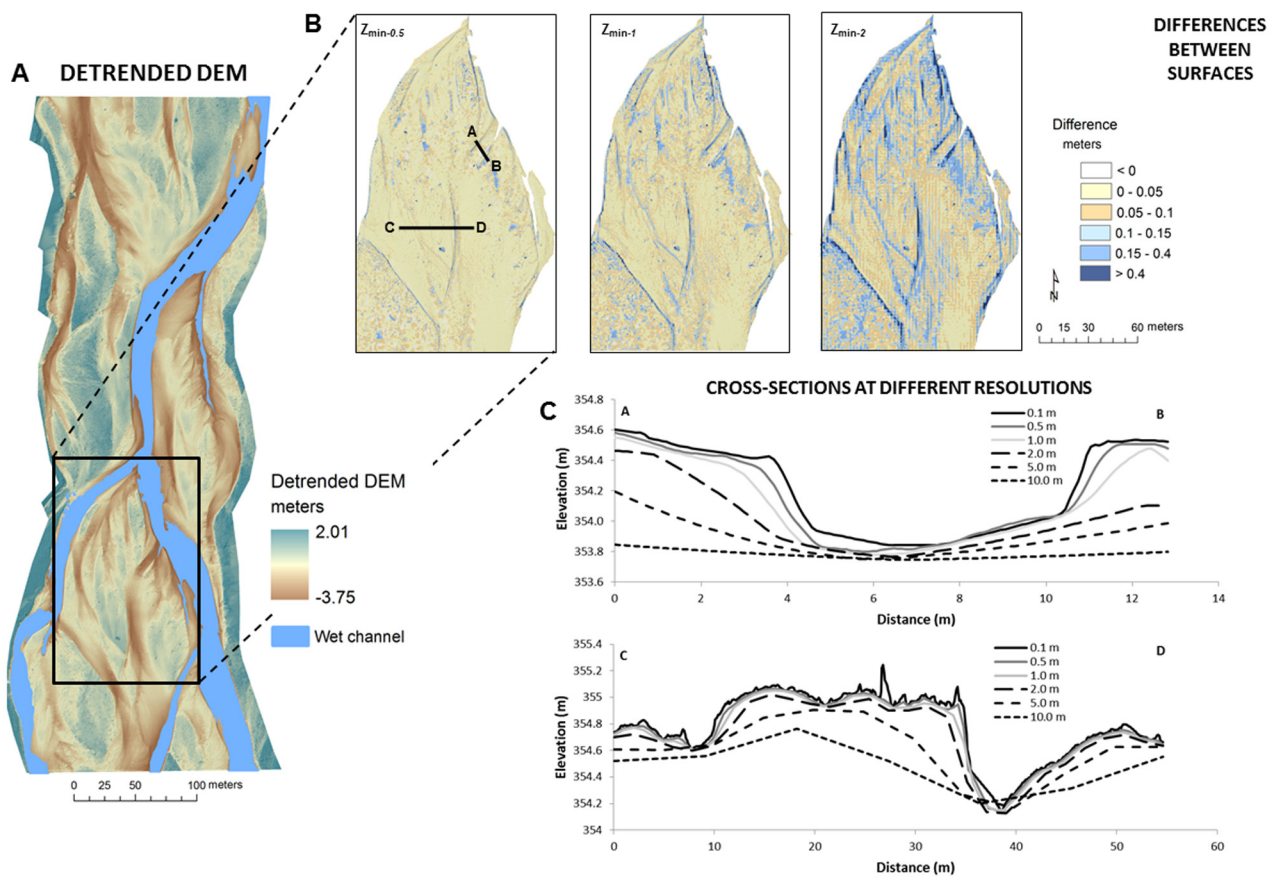

Figure 10.   Progressive generalization of DEMs with decreasing grid resolution: (a) detrended DEM at 0.1 m resolution; (b) high resolution of the box in Figure 10a revealing differences between the 0.1 m DEM and models at 0.5, 1.0, and 2.0 m grid sizes; (c) degradation of cross sections A-B and C-D, plotted as DEM grid-size increases (sections plotted with nondetrended, raw elevation data).

with 2-D modeling results by *McMillan and Brasington* [2007] in their examination of the sensitivity of an urban flood inundation model to grid resolution.

[44] A likely strategy to offset these effects, where empirical data on the extent of flood inundation or water level are available, is the calibration of an effective friction factor (e.g., Manning's *n* or roughness length) that implicitly compensates for the loss of topographically induced flow resistance and steering. However, in the absence of such observations, the parameterization of the roughness should be considered highly uncertain and a complex function of the grid resolution and actual topographic complexity and also hydrodynamic factors such as flow depth.

[45] These results also indicate the likely sensitivity of change detection results to grid size. As the sampling interval increases, the accurate delineation of sharp bank lines is lost and near vertical slopes reduced to gradually sloping banks even at moderately high resolutions, e.g., 1 m. In the case where bank retreat is associated with slumping, the likely result is a significant underestimate in the volume of bank loss. However, at very high resolutions such as the 0.1 m, the extracted cross sections reveal highly complex boundaries which are appear to contain "above surface" features, such as vegetation (see the irregularities in the cross sections extracted at this resolution in Figure 10). Where these objects are transient, such as deciduous vegetative growth, or organic deposits of failed bank material (common on the Feshie), the inclusion of these objects within a DEM of difference is likely to overestimate the predicted volume of change.

[46] These results point toward a complex sensitivity of derived results to grid resolution. While this result is not by itself novel, the high spatial resolution and vertical precision of TLS allow for the first time, effective quantification of the likely impacts of terrain generalization. More significantly still, processing these data using ToPCAT provides opportunities to parsimoniously represent and use this otherwise lost information creatively; for example, by parameterizing a subgrid porosity function for hydraulic models, or modeling the statistical distributions of subgrid elevations to define more robust statistical methods of change detection.

5.2. Intercomparison of TLS and GPS DEMS

[47] In order to evaluate the presence of systematic differences both between survey methods and also spatially within the TLS data set, a direct comparison of TLS and GPS terrain models was undertaken for 1 m resolution models. This analysis was performed for two TLS models; derived from the minimum and mean elevations, respectively. The comparison to GPS surfaces was restricted to the

1 m resolution surfaces as the density of GPS observations is insufficient to justify interpolation to higher resolutions.

[48] Differences between the GPS and TLS models were determined by simply subtracting the grids of the same resolution ($TLS_{x,y} - GPS_{x,y}$), after establishing the origins were coincident. The same GPS-based vertical datum was used to register the TLS data (vertical and horizontal error = 7 mm in the vertical), so any differences between the models should reflect a combination of spatial sampling and processing, the measurement method (i.e., observables, accuracy, and precision) and subsequent interpolation, rather than a datum shift. The results are tabulated in Table 2 and spatial patterns of difference plotted in Figure 11 (note positive differences reflect higher TLS elevations).

[49] While neither the GPS nor TLS-derived models can be treated as true or reference surfaces, the intercomparison yields the expected result that TLS generates a positive bias in the surface elevations as a result of laser returns from above ground features, in particular vegetation. Deviations between the minimum elevation TLS model and GPS model are, however, significantly less (+5 cm) than those obtained for the mean elevation TLS model (+17 cm) suggesting that this simple filtering provides a useful first-order bare earth topography. Nonetheless, large areas of this model incorporate significant positive bias (along the true right bank terrace and on high exposed left bank bars) resulting from a failure to penetrate the vegetation cover, despite the high sampling resolution and small laser spot size (<6 mm at 50 m range). An improved estimate of bare earth elevation may be possible by extending the search radius (grid-size) or through iterative multiresolution comparisons [e.g., *Priestnall et al.*, 2000], however as illustrated above, this is likely to come at the cost of over-generalizing the very subtle fluvial terrain. This result implies that construction of DEMs to represent the topographic boundary condition in distributed hydraulic models will therefore still require judicious editing to estimate and correct for vegetation heights and that ground-truth data (acquired by GPS for example) is likely to remain necessary to refine and validate the derived products.

[50] There is also some indication that the TLS survey may result in slightly higher elevations even on unvegetated surfaces. For example, the bar head of the most downstream complex bar, marked by the box in Figure 11, comprises exposed sands and gravels, but here the TLS model has a positive bias of between 1 and 10 cm. Such differences result from the noninvasive laser beam recording the tops of individual clasts, while the GPS survey, which was undertaken using a pointed detailed pole, is more likely to sample interstitial elevations. Such positively biased sampling with TLS will increase with distance to the scan origin, reflecting lower and lower angles of incidence of the laser beam so

Table 2. Descriptive Statistics (Including the 5% and 95% Confidence Intervals) of the Difference Between DEMS Based on TLS and GPS Data[a]

Elevation Metric Used to Derive TLS-DEM (Z_i)	Difference [Z_i − GPS] at 1 m Grid Cell							
	Mean (m)	Maximum (m)	Minimum (m)	Median (m)	5% (m)	95% (m)	Standard Deviation (m)	*n* Obs.
Minimum	0.05	1.46	−3.92	0.04	−0.09	0.26	0.13	81,658
Mean	0.17	1.99	−0.61	0.13	0.03	0.42	0.14	81,658

[a]Results shown for TLS DEMs derived using both the grid mean and grid minimum elevation values.
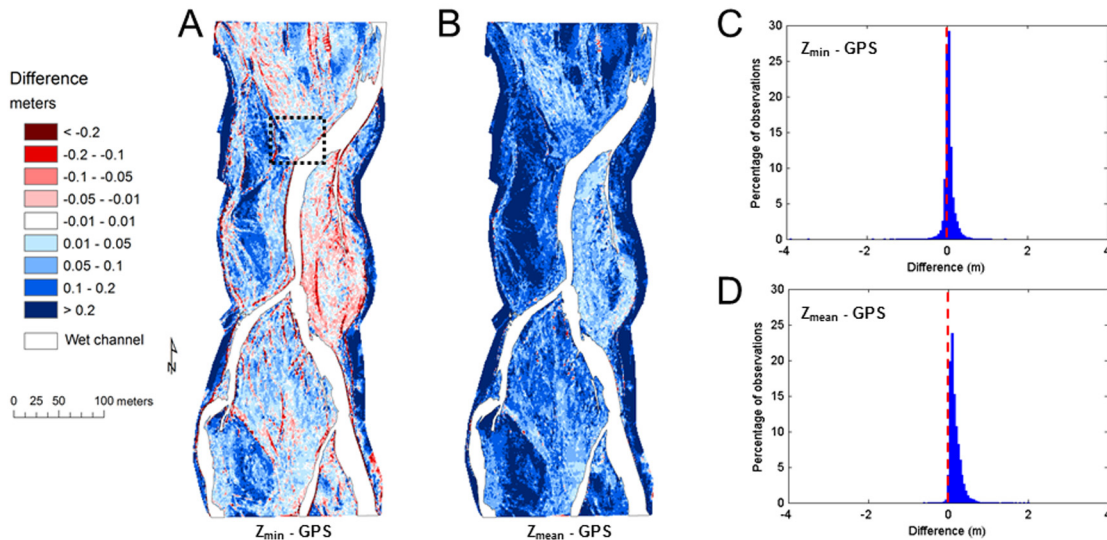
Figure 11. Maps showing the elevation differences between DEMs derived from TLS and GPS survey data. (a) Differences for the TLS DEM derived using the grid minimum; (b) differences for the TLS mean elevation model; (c and d) the corresponding frequency distribution of differences for the Z_{min} and Z_{mean} models, respectively. The dotted box shows an area of TLS positive anomalies on an exposed gravel bar head.

that occlusions along the beam path preclude data returns from the surficial interstices.

[51] Finally, close inspection of the minimum elevation – GPS model comparison also indicates that in areas close to sharp banks, the TLS model actually predicts lower elevations that those obtained by GPS. This reflects the precise delineation of the bank line with TLS and a likely undersampling of such sharp discontinuities by the manual GPS survey. While every attempt was made to survey breaks-of-slope with the GPS, the low spatial frequency of observations (a point density of <0.17 pts m^{-2} compared with 0.94 pts m^{-2} at 1 m resolution for the TLS) inevitably yields a more generalized surface. This is likely to have important implications when comparing DEMs of difference derived from GPS-GPS or TLS-TLS models, with the former prone to underestimating bank scour and dissection of bar surfaces by small (1–3 m) chutes which lie below the sampling resolution of the input data.

6. Retrieving Particle-Size Information From Subgrid Topography

[52] Methods for the automated retrieval of particle size and facies information from remotely sensed data have, to date, largely relied on texture mapping from high resolution optical imagery [e.g., *Carbonneau et al.*, 2004; *Verdu et al.*, 2005]. While such methods can yield detailed, spatially continuous data, the results are strongly dependent on particle sorting, scene illumination, and require very high resolution (cm scale) imagery. Recent research has demonstrated that that an explicitly topographic approach to retrieving particle size information may be possible using data acquired by TLS. *Entwistle and Fuller* [2009] and *Heritage and Milan* [2009] both used submeter convolution kernels to determine the local standard deviation of elevations from centimeter resolution DEMs of gravel bars and

correlated the results with surface particle size measurements. While promising, this approach fails to account for scale dependence of the resulting elevation statistics, which even at submeter resolution, are likely to incorporate topographic signatures of bed forms, banks, and avalanche faces in addition to grain size.

[53] The detrending procedure implemented in ToPCAT is designed specifically to reduce these effects by fitting a lower frequency surface across each gridcell which is used to eliminate topographic trends at or above the grid resolution. Moreover, unlike the approaches described above, the statistical decomposition is based directly on the raw point cloud rather than a DEM and therefore: (1) does not incorporate artifacts introduced during interpolation; particularly those associated with rendering a 3-D point cloud into a 2.5-D triangulation or raster data structure; and (2) does not require computationally expensive prior interpolation, limiting the spatial extent of analysis, when by contrast, ToPCAT has been used successfully on data sets exceeding 10^9 observations.

[54] To examine the relationship between the detrended topography and the surface particle size, 12 pebble counts were collected across the study reach, designed to capture the variability of surface facies. Grid-by-number sampling [*Bunte and Apt*, 2001] was used to estimate particle size on patches varying between 1 and 4 m^2 according to the maximum individual clast size. The a, b, c axes of the grains were measured and D_{50}, D_{16}, and D_{84} determined. The median b axis, varied between 33 to 117 mm. The four corners of each patch were measured using GPS and these locations used to clip the point cloud to the exact position each of each pebble count. The standard deviation of elevation was then computed before (σ_z) and after detrending (σ_{dz}) the clipped point clouds; here, linear orthogonal regression was used to fit a plane to the local slope by principal components analysis and the residuals of each point from this

Table 3. Median Particle Size and Corresponding Grid Statistics for Selected Patches in the River Feshie[a]

Sample	Median Particle Size D_{50} (mm)	SD of Elevation (σ_z)	
		Raw (mm)	Detrended (mm)
Patch 1	30.3	9.4	8.6
Patch 2	41.8	12.4	11.6
Patch 3	43.9	20.4	15.5
Patch 4	49.8	17.4	13.5
Patch 5	59.5	15.3	15
Patch 6	74.6	53.1	22.5
Patch 7	82.4	50.1	32.4
Patch 8	91.9	37	30.4
Patch 9	92.8	33.3	31.5
Patch 10	92.8	34.1	33.5
Patch 11	99.9	88.6	35
Patch 12	117.4	36.1	34.3

[a]Statistical relations are also presented in Figure 12.

plane calculated. Statistics of the pebble data, raw and detrended point clouds of each patch are given in Table 3.

[55] Figure 12a shows the relationship between the observed median surface particle size (D_{50}, mm) and the extracted standard deviation for both the raw and detrended (σ_z and σ_{dz}, mm) point clouds. The relationship between the raw standard deviation and particle size appears to reveal two distinct relationships characterized by different gradients and intercepts. On detrending, these collapse on to one curve, describing a strong linear relationship, parameterized by a near zero intercept (12 mm) and a gradient of 2.59 ($r^2 = 0.92$, $p < 0.001$). Figure 12b extends this analysis by incorporating comparable particle size and laser scan data from two more settings, Tan y Bwlch beach in West Wales (UK) dominated by coarse rounded grains ($D_{50} = 70$ mm), and the Rees River, Otago (NZ), which is characterized by platy, schistose, finer grained sediments ($D_{50} = 9$–35 mm). The addition of these samples from different contexts emphasizes the value of detrending the point, resulting in a significant reduction in scatter and an improvement in r^2 from 0.45 to 0.95. The resulting relationship between

detrended standard deviation and particle size is very similar to that obtained just for the Feshie, although with a slight improvement in the overall goodness of fit (intercept = -4 mm; gradient = 3.08; $r^2 = 0.95$, $p < 0.001$).

[56] The identification of a robust relationship between σ_{dz} and particle size offers significant promise for mapping the reach-scale distribution of facies and related roughness characteristics. These results also emphasize the importance of detrending the local topography before extracting relevant elevation statistics; confirming the likely spatial-scale dependence of the particle-size estimates. It is important to note however, that separation of the overlapping scales of particle bed form-bar form topographies may not always be easily achieved using the grid-based discretization strategy employed here. For example, at discretizations of 0.5–l m, ripples in patches of sand will give rise to σ_{dz} similar to coarse gravels or cobbles, similarly larger bed forms, including particle clusters, gravel dunes, and anti-dunes, may also influence the predicted grain size albeit at larger scales of spatial decomposition.

[57] Despite the problematic overlap between grain and bed form topographies, this approach provides a means to map reach-scale patterns continuously and at very high resolution, as shown in Figure 13. Here, areas where σ_{dz} exceeds that of the coarsest particles were taken to be vegetation. The complexity of spatial patterning obtained is realized in the close-up inset image, which compares the predicted distribution of facies with a close-range vertical aerial image (5 cm raw pixel resolution). The boundary between fine gravel/sand and cobble facies is well demarcated, as is the vegetated high surface on the true left. It is, however, also noteworthy that discrete units of failed bank material are also clearly identified, although predicted to be coarse cobbles rather than organic rich bank top material. Nonetheless, such data provide a useful first order approximation which may be appropriate for mapping roughness lengths using a simple multiplier approach [Clifford et al., 1992].

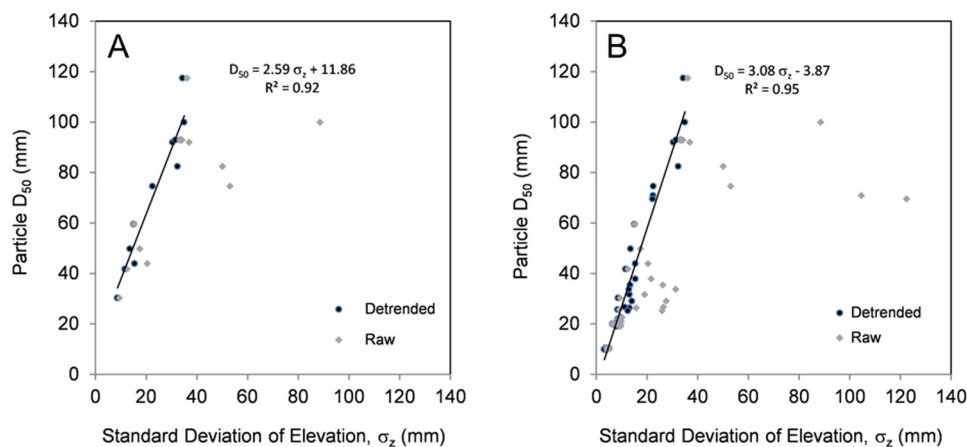[58] While this approach to estimating particle size or roughness may provide a ready tool for parameterizing

Figure 12. Relationship between median surface particle size (D_{50}) and the standard deviation of local elevations. Gray and blue observations correspond to moments of the elevation distribution derived from the raw and detrended TLS data respectively. (a) The relationship for particle size data from the River Feshie (see also Table 3). (b) Additional data incorporated from the Tan y Bwlch and the Rees River. Regression results correspond to the detrended data models.
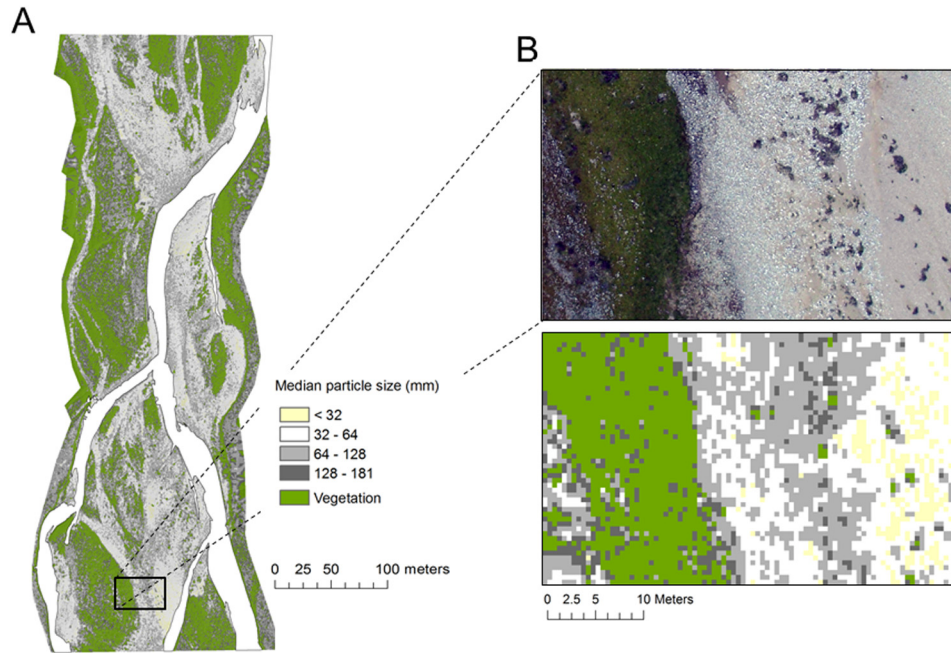
Figure 13. Derived maps of reach-scale facies and vegetation cover on the River Feshie. Figure 13b reveals local sorting patterns at the bar scale.

flow resistance terms in existing hydraulic models, the very high resolution topography may actually be more usefully employed in more complex methods of spatial decomposition. For example wavelet or Fourier transforms could be used to capture the full power spectrum of topography, offering the possibility to reconstruct the topography formally as a continuous, scale-dependent function. Similarly, the subgrid elevations could be used to predict, deterministically or statistically, the local surface porosity as described in section 5 above.

7. Discussion: Challenges and Prospects

[59] The horizons of terrain modeling have been stretched repeatedly over the last 15 years through progressive developments in geomatics. For a study site like the Feshie described here, these advances have resulted in a six order of magnitude enhancement in data density; as sparsely sampled cross sections (comprising 10^2 points) have been replaced by distributed ground surveys (e.g., GPS as used here, comprising 10^4 points), airborne LiDAR and photogrammetry, (providing 10^5 points) and now TLS with the capacity to generate centimeter resolution data sets comprising 10^8 observations. It could be argued that this empirical revolution has outstripped the pace of more fundamental developments in theory and modeling, so that our existing armory of tools to explore and predict fluvial responses have yet to take full advantage of the extreme data resolutions now available.

[60] Intelligent data decimation procedures such as ToPCAT provide a versatile means of capturing and representing these emerging data-streams in parsimonious, but novel geospatial products suitable for assimilation in existing frameworks for hydrodynamic modeling and geomorphological change detection. Performance tests on the distribution version of the code reveal its suitability for desktop deployment without the need for high performance computing. For example, processing the 178 million point data set at the highest 0.1 m resolution, on a laptop PC with a moderate specification (Intel Core Duo 2.53 GHz processor, 8 GB of RAM, Windows 7 ×64) required 22:32 min processing time. This run time was largely associated with input-output operations (and thus strongly linked to the output grid size and storage media speed) and the sorting operations were completed in only 147 s. Batch processing (analyzing the same file at multiple resolutions simultaneously) results in significant runtime gains, as the input data file is read only once, reducing runtimes by well over 50%.

[61] However, while TLS based data sets offer exciting new opportunities, there remain a number of challenges that require further research and development. Primary among these is the inability to survey wetted channels due to the rapid attenuation and absorption of the green, red, and near infrared lasers used in TLS. Water penetrating lasers suitable for bathymetric survey, such as the experimental advanced airborne research LiDAR [McKean et al., 2009] have been developed for airborne platforms, however the power output necessary for deep (>1 m) water penetration of the shortwave (532 nm) lasers used makes the approach inappropriate for high focused (2–4 mm spot size) ground-based lasers. Consequently, the production of continuous fluvial terrain models requires a data fusion approach, integrating information acquired through TLS with secondary bathymetric surveys. The new generation of multibeam echo sounders with data resolutions and precision comparable to TLS [e.g., Parsons et al., 2005] are ideally suited to this purpose, although at present are restricted to deployment in relatively deep (>1 m) navigable water bodies and inappropriate in shallow gravel bed rivers such as reported here. In these circumstances, commonly employed fall-backs involve ground-based surveys of wadeable streams

or the calibration of an optical depth model from aerial photography [e.g., *Brasington et al.*, 2003]. Such data are typically of much lower resolution and precision, ultimately degrading the unified data product and in many cases, in the most sensitive areas of the system. An exciting possible solution to this conundrum lies in the deployment of lightweight, acoustic Doppler current profilers such as the Sontek S5 or M9. These instruments have multiple (5–9) sonic transducers from which estimates of bed depth can be derived, even in very shallow waters (10 cm depth). Such highly portable instruments can be mounted on small (submeter) tethered or remote control boats and when coupled with an external differential GPS, can be used to map the bed at high temporal frequency (observations acquired at 10 Hz), resulting in dense spatial mapping as the boat moves (see *Brasington et al.* [2011] for further details).

[62] The next most significant challenge now lies in expanding the spatial coverage of TLS. The survey described here required 18 individual setups, each requiring approximately 2–3 h of occupation time to scan the scene and record the targets. As with any emerging technology, the pace of advance has been significant and the current generation of TLS have dramatically enhanced ranges and survey frequency reducing data acquisition times. The recently released Leica HDS7000 phase-based scanner, for example, has a peak frequency of 10^6 points per second and a range of 182 m. However, the most significant gains are likely to emerge through the integration of TLS with navigation systems, tracking the position and attitude of a scanner on a moving platform. This enables scans to be acquired from moving platforms, such as boats, cars, or trains. *Brasington* [2010] [see also *Williams et al.*, 2011] described the application of a mobile TLS system deployed on an amphibious all-terrain vehicle to survey an extensive 3 × 0.7 km reach of the Rees River in Otago, NZ. This ruggedized platform also employs optical navigation and GPS to orientate and position the scanner, resulting in dramatically reduced survey times. Using this mobile system, they were able to acquire very high resolution (up to 5 cm) terrain models of a large, dynamic braidplain between frequent channel forming events in the New Zealand summer flood season. These data sets comprised over 6,000,000,000 individual *xyz* survey observations and were processed using ToPCAT to generate high quality terrain products such as shown in Figure 14.

[63] Similar systems mobile systems have been developed for boat-based platforms [*Alho et al.*, 2009] and road vehicles [*Barber et al.*, 2008]. However, while the scope of such kinematic laser scanner systems dramatically enhances potential coverage, the dependence on direct georeferencing using real-time GPS and inertial or optical navigation units results in less reliable and lower density data that could be acquired from static deployments. Ultimately, the appropriate survey
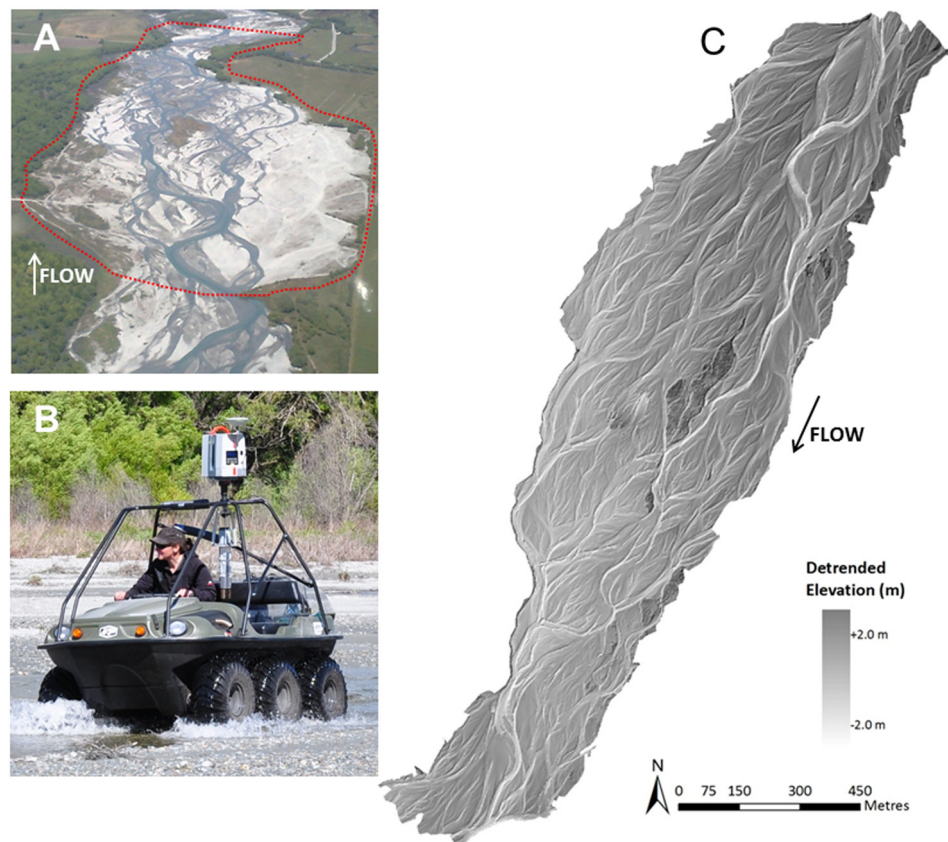

Figure 14. Hyperscale modeling of the braided Rees River, NZ. (a) 3 km study reach; (b) mobile terrestrial laser survey system in the field; and (c) 0.5 m resolution DEM derived from a 6 × 10^9 point cloud.

method must been targeted to the goals of the application and a trade-off between data resolution, observation quality, and spatial extent must be effectively closed.

8. Conclusions

[64] A novel, intelligent decimation algorithm to process high density TLS data sets has been presented and evaluated. The algorithm is available in a distributable form as a simple toolbox. In this paper we have shown the approach to offer a number of significant opportunities, including:

[65] 1. Computationally efficient processing of very large topographic data sets on desktop PCS.

[66] 2. Decimation of dense point cloud data into reduced resolution statistical summaries that retain information on the subgrid topographic variability.

[67] 3. Simple measures for regional estimation of bare-earth topography from dense first pulse scan data.

[68] 4. The generation of subgrid terrain products suitable for visualization and mapping in GIS.

[69] 5. Identification of key spatial scale dependencies in fluvial terrain models.

[70] 6. The quantification of lost topographic information as DEM resolution is degraded.

[71] 7. Inferred impacts for numerical hydrodynamic modeling and change detection analysis as DEM grid size is degraded.

[72] 8. Dense spatial mapping of fluvial facies using locally detrended moments of the elevation distribution.

References

Alho, P., A. Kukko, H. Hyyppä, H. Kaartinen, J. Hyyppä, and A. Jaakkola (2009), Application of boat-based laser scanning for river survey, *Earth Surf. Processes Landforms, 34*, 1831–1838, doi:10.1002/esp.1879.

Antonarakis, A. S., K. S. Richards, J. Brasington, and M. Bithell (2009), Leafless roughness of complex tree morphology using terrestrial LiDAR, *Water Resour. Res., 45*, W10401, doi:10.1029/2008WR007666.

Antonarakis, A. S., K. S. Richards, J. Brasington, and E. Muller (2010), Determining LAI and leafy tree roughness using terrestrial laser scanning, *Water Resour. Res., 46*, W06510, doi:10.1029/2009WR008318.

Aryal, A., B. A. Brooks, M. E. Reid, G. W. Bawden, and G. Pawlak (2012), Displacement fields from point cloud data: application of particle imaging velocimetry to landslide geodesy, *J. Geophys. Res.*, doi:10.1029/2011JF002161, in press.

Ashmore P. E., and M. Church (1998), Sediment transport and river morphology: A paradigm for study, in *Gravel-Bed Rivers in the Environment*, edited by R. D. Hey, J. C. Bathurst, and C. R. Thorne, pp. 115–148, Wiley, Chichester.

Barber, D., J. Mills, and S. Smith-Voysey (2008), Geometric validation of a ground-based mobile laser scanning system, *ISPRS J. Photogram. Remote Sensing, 63*, 128–141.

Barnes, H. H. (1967), Roughness characteristics of natural channels, *U.S. Geological Survey Water-Supply Paper 1849*, 213 pp.

Bates, P. D., K. J. Marks, and M. S. Horritt (2003), Optimal use of high-resolution topographic data in flood inundation models, *Hydrol. Processes 17*, 5237–5557.

Besl, P. J., and N. D. McKay (1992), A method for registration of 3-D shapes, *IEEE Trans. Pattern Anal. Machine Intel., 14*, 239–256.

Brasington, J. (2010), From grain to floodplain: Hyperscale models of braided rivers, *J. Hydraul. Res., 48*(4), 52–53, Suppl. 4.

Brasington, J., and K. S. Richards (1998), Interactions between model predictions, parameters and DTM scales for TOPMODEL, *Comput. Geosci., 24*, 299–314.

Brasington, J., B. T. Rumsby, and R. McVey (2000), Monitoring and modelling morphological change in braided river systems using the Global Positioning System, *Earth Surf. Processes Landforms, 25*, 973–990.

Brasington, J., J. Langham, and B. T. Rumsby (2003), Three-dimensional channel sediment budgets: methodological sensitivity of remote survey methods, *Geomorphology, 53*, 299–316.

Brasington, J., C. D. Rennie, D. Vericat, R. Williams, B. Goodsell, M. Hicks, and R. Batalla (2011), Monitoring braided river morphodynamics with an acoustic Doppler current profiler, in *Proceedings of the 34th World Congress of the International Association for Hydro-Environment Research and Engineering*, edited by E. M. Valentine et al., pp. 3396–3403, Engineers Australia.

Brodu, N., and D. Lague (2012), 3-D Terrestrial LiDAR data classification of complex natural scenes using a multi-scale dimensionality criterion: Applications in geomorphology, *ISPRS J. Photogram. Remote Sensing, 68*, 121–134.

Buckley, S. J., J. A. Howell, H. D. Enge, and T. H. Kurz (2008), Terrestrial laser scanning in geology: Data acquisition, processing and accuracy considerations, *J. Geol. Soc., 165*, 625–638.

Bunte, K., and S. R. Apt (2001), Sampling surface and subsurface particle-size distributions in wadable gravel- and cobble-bed streams for analysis in sediment transport, hydraulics, and streambed monitoring, General Technical *Rep. RMRS-GTR-74*, U.S. Dept. of Agriculture, Forest Service, Rocky Mountain Forest and Range Experimental Station, Fort Collins, Colorado, 428 pp.

Carbonneau P. E., S. N. Lane, and N. E. Bergeron (2004), Catchment-scale mapping of surface grain size in gravel-bed rivers using airborne digital imagery, *Water Resour. Res., 40*, W07202, doi:10.1029/2003WR002759.

Casas, M. A., S. N. Lane, R. J. Hardy, G. Benito, and P. J. Whiting (2010), Reconstruction of subgrid-scale topographic variability and its effect upon the spatial structure of three-dimensional river flow, *Water Resour. Res., 46*, W03510, doi:10.1029/2009WR007756.

Clifford, N. J., A. Robert, and K. S. Richards (1992), Estimation of flow resistance in gravel-bed rivers: A physical explanation of the multiplier of roughness length, *Earth Surf. Processes Landforms, 17*, 111–126.

Danson, F. M., D. Hetherington, F. Morsdorf, B. Koetz, and B. Allgöwer (2007), Three-dimensional forest structure from terrestrial laser scanning, *IEEE Geosci. Remote Sensing Lett., 4*, 157–160

Dunning, S. A., N. J. Rosser, and C. I. Massey (2010), The integration of terrestrial laser scanning and numerical modelling in landslide investigations, *Q. J. Eng. Geol. Hydrogeol.. 43*, 233–247.

Eaton, B. C., and M. F. Lapointe (2001), Effects of large floods on sediment transport and reach morphology in the cobble-bed Sainte Marguerite River, *Geomorphology, 40*, 291–309.

Entwistle, N. S., and I. C. Fuller (2009), Terrestrial laser scanning to derive surface grain size facies character of gravel bars, in *Laser Scanning for the Environmental Sciences*, edited by G. L. Heritage and A. R. G. Large, Wiley-Blackwell, Oxford, UK.

Franceschi, M., G. Teza, N. Preto, A. Pesci, A. Galgaro, and S. Girardi (2009), Discrimination between marls and limestones using intensity data from terrestrial laser scanner, *ISPRS J. Photogram. Remote Sensing, 64*, 522–528.

Gao, J. (2009), Bathymetric mapping by means of remote sensing: methods, accuracy and limitations, *Progress Phys. Geogr., 33*, 103–116.

Grohmann, C. H., M. J. Smith, and C. Riccomini (2010), Multi-scale analysis of surface roughness, *IEEE Trans. Geosci. Remote Sensing, 99*, 1–14.

Heritage, G. L., and A. R. G. Large (2009), *Terrestrial Laser Scanning for the Environmental Sciences*, 288 pp., Wiley-Blackwell, Chichester.

Heritage, G. L., and D. Hetherington (2007), Towards a protocol for laser scanning in fluvial geomorphology, *Earth Surface Processes and Landforms, 32*, 66–74.

Heritage, G. L., and D. J. Milan (2009), Terrestrial laser scanning of grain roughness in a gravel-bed river, *Geomorphology, 113*, 4–11.

Hicks, D. M., and P. J. Mason (1991), Roughness characteristics of New Zealand rivers, in *New Zealand Water Resources Survey*, p. 329, DSIR Marine and Freshwater, Wellington.

Hodge R. A., J. Brasington, and K. S. Richards (2009a), Characterisation of grain-scale fluvial morphology using TLS, *Earth Surf. Processes Landforms, 34*, 954–968.

Hodge R. A., J. Brasington, and K. S. Richards (2009b), Analysing laser-scanned digital terrain models of gravel bed surfaces: Linking morphology to sediment transport processes and hydraulics, *Sedimentology*, *56*, 2024–2043.

Horn, B. K. P. (1987), Closed-form solution of absolute orientation using unit quaternions, *J. Opt. Soc. Am. A*, *4*(4), 629–642.

Horritt, M. S., and P. D. Bates (2002), Evaluation of l-D and 2-D numerical models for predicting river flood inundation, *J. Hydrol.*, *268*, 87–99.

James, M. R., H. Pinkerton, and L. J. Applegarth (2009), Detecting the development of active lava flow fields with a very-long-range terrestrial laser scanner and thermal imagery, *Geophys. Res. Lett.*, *36*, L22305, doi:10.1029/2009GL040701.

Jenness, J. S. (2004), Calculating landscape surface area from digital elevation models, *Wildlife Soc. Bull.*, *32*, 829–839.

Lane, S. N. (2005), Roughness—time for a re-evaluation? *Earth Surf. Processes Landforms*, *30*, 251–253.

Lane, S. N., R. J. Hardy, L. Elliott, and D. B. Ingham (2004), Numerical modeling of flow processes over gravelly surfaces using structured grids and a numerical porosity treatment, *Water Resour. Res.*, *40*, W01302, doi:10.1029/2002WR001934.

Lichti, D. D. (2005), Spectral filtering and classification of terrestrial laser scanner point clouds, *Photogram. Rec.*, *20*, 218–240.

Lichti, D. D., and S. Jamtsho (2006), Angular resolution of terrestrial laser scanners, *Photogram. Rec.*, *21*, 141–160.

Lichti, D. D., and J. Skaloud (2010), Registration and calibration, in *Airborne and Terrestrial Laser Scanning*, edited by G. Vosselman and H.-G. Maas, pp. 83–133, Whittles, Caithness, UK.

Lichti, D. D., S. J. Gordon, and M. P. Stewart (2002), Ground-based laser scanners: operations, systems and applications, *Geomatica*, *56*, 21–33.

Lichti, D. D., N. Pfeifer, and H.-G. Maas (2008), Editorial: ISPRS Journal of Photogrammetry and Remote Sensing theme issue "Terrestrial laser scanning," *ISPRS J. Photogram. Remote Sensing*, *63*, 1–3.

Marcus, W. A., and M. A. Fonstad (2010), Remote sensing of rivers: The emergence of a subdiscipline in the river sciences, *Earth Surf. Processes Landforms*, *35*, 1867–1872.

McKean, J., D. Isak, and W. Wright (2009), Improving stream studies with a small- footprint green LiDAR, *Eos Trans. AGU. 90*, 341–342.

McMillan, H. K., and J. Brasington (2007), Reduced complexity strategies for modelling urban floodplain inundation, *Geomorphology*, *90*, 226–243.

Milan, D. J., D. Hetherington, and G. L. Heritage (2007), Application of a 3-D laser scanner in the assessment of erosion and deposition volumes and channel change in a proglacial river, *Earth Surface Processes Landforms*, *32*, 1657–1674.

Nield, J. M., and G. F. S. Wiggs (2011), The application of terrestrial laser scanning to aeolian saltation cloud measurement and its response to changing surface moisture, *Earth Surf. Processes Landforms*, *36*, 273–278.

Parsons, D., J. L. Best, R. J. Hardy, R. A. Kostaschuk, S. N. Lane, and O. Orfeo (2005), The morphology and flow fields of three-dimensional dunes, Rio Paraná, Argentina: Results from simultaneous multibeam echo sounding and acoustic Doppler current profiling, *J. Geophys. Res.*, *110*, F04S03, doi:10.1029/2004JF000231.

Petrie, G., and C. K. Toth (2008), Introduction to laser ranging, profiling, and scanning, in *Topographic Laser Ranging and Scanning: Principles and Processing*, edited by J. Shan and C. K. Toth, 590 pp., CRC, Taylor & Francis, London.

Priestnall, G., J. Jaafar, and D. Duncan (2000), Extracting urban features from LiDAR digital surface models, *Comput. Environ. Urban Syst.*, *24*, 65–78.

Richards, K. S., J. Brasington, and F. R. M. Hughes (2002), Geomorphic dynamics of floodplains: Ecological implications, *Freshwater Biol.*, *47*, 559–579.

Rychkov, I., J. Brasington, D. Vericat (2012), Computational and methodological aspects of terrestrial surface analysis based on point clouds, *Computers and Geosciences*, *42*, 64–70.

Verdu J. M., R. J. Batalla, and J. A. Martinez-Casasnovas (2005), High-resolution grain-size characterisation of gravel bars using imagery analysis and geostatistics, *Geomorphology*, *72*, 73–93.

Vosselman, G., and H. G. Mass (2010), *Airborne and Terrestrial Laser Scanning*, Whittles, Scotland, UK.

Wang, C.-K., and G.-H. Huang (2012), Multi-scale geostatistical estimation of gravel-bed roughness from terrestrial and airborne laser scanning, *IEEE Geosci. Remote Sensing Lett.*, *9*, 1084–1088, doi:10.1109/LGRS. 2012.2189351.

Wang, C.-K., F.-C. Wu, G.-H. Huang, and C.-Y. Lee (2011), Mesoscale terrestrial laser scanning of fluvial gravel surfaces. *IEEE Geosci. Remote Sensing Lett.*, *8*, 1075–1079.

Wehr, A., and U. Lohr (1999), Airborne laser scanning—An introduction and overview, *ISPRS J. Photogram. Remote Sensing*, *54*, 68–82.

Weiss, M. A. (2007), *Data Structures and Algorithms in C++*, 3rd ed., 586 pp., Addison-Wesley, Reading, MA.

Westaway R. M., S. N. Lane, and D. M. Hicks (2003), Remote survey of large-scale braided rivers using digital photogrammetry and image analysis, *Int. J. Remote Sensing 24*, 795–816.

Westoby, M. J., J. Brasington, N. F. Glasser, M. J. Hambrey, and J. M. Reynolds (2012), Structure-from-motion photogrammetry: A low-cost, effective tool for geoscience applications, *Geomorphology*, doi:10.1016/ j.geomorph.2012.08.021, in press.

Wheaton, J., J. Brasington, S. E. Darby, and D. Sear (2010a), Accounting for uncertainty in DEMs from repeated topographic survey: improved sediment budgets, *Earth Surf. Processes Landforms*, *35*, 136–156.

Wheaton, J., J. Brasington, S. E. Darby, J. Mertz, G. B. Pasternack, D. Sear, and D. Vericat (2010b), Linking geomorphic changes to salmonid habitat and a scale relevant to fish, *River Res. Appl.*, *26*, 469–486.

Williams, R. D., J. Brasington, D. Vericat, D. M. Hicks, F. Labrosse, and M. Neal (2011), Monitoring braided river change using terrestrial laser scanning and optical bathymetry, in *Geomorphological Mapping: Methods and Applications*, edited by M. Smith, P. Paron, and J. Griffiths, pp. 508–529, Elsevier, New York.

Yu, D., and S. N. Lane (2006), Diffusion-based modeling of flood inundation based on sub-grid connectivity, in *River Flow* 2006, edited by R. M. L. Ferreira, et al., pp. 313–322, Taylor Francis, London.